CrossMark

Detection of the Far-infrared [O III] and Dust Emission in a Galaxy at Redshift 8.312: Early Metal Enrichment in the Heart of the Reionization Era

Yoichi Tamura[1] , Ken Mawatari[2,3], Takuya Hashimoto[2,4] , Akio K. Inoue[2] , Erik Zackrisson[5] , Lise Christensen[6] ,
Christian Binggeli[5], Yuichi Matsuda[4,7], Hiroshi Matsuo[4,7], Tsutomu T. Takeuchi[1], Ryosuke S. Asano[1], Kaho Sunaga[1],
Ikkoh Shimizu[8], Takashi Okamoto[9], Naoki Yoshida[10,11], Minju M. Lee[1,4] , Takatoshi Shibuya[12], Yoshiaki Taniguchi[13] ,
Hideki Umehata[13,14,15] , Bunyo Hatsukade[15] , Kotaro Kohno[15,16] , and Kazuaki Ota[17,18]

[1] Division of Particle and Astrophysical Science, Graduate School of Science, Nagoya University, Nagoya 464-8602, Japan; ytamura@nagoya-u.jp
[2] Department of Environmental Science and Technology, Faculty of Design Technology, Osaka Sangyo University, 3-1-1, Nakagaito, Daito, Osaka 574-8530, Japan
[3] Institute for Cosmic Ray Research, The University of Tokyo, Kashiwa, Chiba 277-8582, Japan
[4] National Astronomical Observatory of Japan, 2-21-1, Osawa, Mitaka, Tokyo 181-8588, Japan
[5] Observational Astrophysics, Department of Physics and Astronomy, Uppsala University, Box 516, SE-751 20 Uppsala, Sweden
[6] Dark Cosmology Centre, Niels Bohr Institute, University of Copenhagen, Juliane Maries Vej 30, DK-2100 Copenhagen, Denmark
[7] The Graduate University for Advanced Studies (SOKENDAI), 2-21-1, Osawa, Mitaka, Tokyo 181-8588, Japan
[8] Department of Earth & Space Science, Osaka University, 1-1, Machikaneyama, Toyonaka, Osaka 560-0043, Japan
[9] Department of Cosmosciences, Graduate School of Science, Hokkaido University, N10W8, Kitaku, Sapporo 060-0810, Japan
[10] Department of Physics, Graduate School of Science, The University of Tokyo, Tokyo 113-0033, Japan
[11] Kavli Institute for the Physics and Mathematics of the Universe (WPI), Todai Institutes for Advanced Study,
The University of Tokyo, Kashiwa, Chiba 277-8583, Japan
[12] Department of Computer Science, Kitami Institute of Technology, 165 Koen-cho, Kitami, Hokkaido 090-8507, Japan
[13] The Open University of Japan, 2-11 Wakaba, Mihama-ku, Chiba 261-8586, Japan
[14] RIKEN Cluster for Pioneering Research, 2-1 Hirosawa, Wako-shi, Saitama 351-0198, Japan
[15] Institute of Astronomy, The University of Tokyo, 2-21-1, Osawa, Mitaka, Tokyo 181-0015, Japan
[16] Research Center for the Early Universe, Graduate School of Science, The University of Tokyo, Tokyo 113-0033, Japan
[17] Kavli Institute for Cosmology, University of Cambridge, Madingley Road, Cambridge, CB3 0HA, UK
[18] Kyoto University Research Administration Office, Yoshida-Honmachi, Sakyo-ku, Kyoto 606-8501, Japan

Abstract

We present the Atacama Large Millimeter/submillimeter Array detection of the [O III] 88 μm line and rest-frame 90 μm dust continuum emission in a Y-dropout Lyman break galaxy (LBG), MACS0416_Y1 lying behind the Frontier Field cluster MACS J0416.1−2403. This [O III] detection confirms the LBG with a spectroscopic redshift of $z = 8.3118 \pm 0.0003$, making this object one of the farthest galaxies ever identified spectroscopically. The observed 850 μm flux density of 137 ± 26 μJy corresponds to a de-lensed total infrared (IR) luminosity of $L_{\rm IR} = (1.7 \pm 0.3) \times 10^{11} L_\odot$ if assuming a dust temperature of $T_{\rm dust} = 50$ K and an emissivity index of $\beta = 1.5$, yielding a large dust mass of $4 \times 10^6 M_\odot$. The ultraviolet-to-far-IR spectral energy distribution modeling where the [O III] emissivity model is incorporated suggests the presence of a young ($\tau_{\rm age} \approx 4$ Myr), star-forming (SFR ≈ 60 $M_\odot$ yr^{-1}), moderately metal-polluted ($Z \approx 0.2 Z_\odot$) stellar component with a mass of $M_{\rm star} = 3 \times 10^8 M_\odot$. An analytic dust mass evolution model with a single episode of star formation does not reproduce the metallicity and dust mass in $\tau_{\rm age} \approx 4$ Myr, suggesting a pre-existing evolved stellar component with $M_{\rm star} \sim 3 \times 10^9 M_\odot$ and $\tau_{\rm age} \sim 0.3$ Gyr as the origin of the dust mass.

Key words: dust, extinction – galaxies: formation – galaxies: high-redshift – galaxies: ISM

1. Introduction

How and when metal enrichment happened in the epoch of reionization (EoR) is one of the most fundamental questions in modern astronomy. Recent *Planck* results suggest that the cosmic reionization occurred at an instantaneous reionization redshift of $z_{\rm re} = 7.68 \pm 0.79$ (Planck Collaboration et al. 2018), and the latest *Hubble Space Telescope* (*HST*) surveys have revealed more than a hundred candidate $z \gtrsim 8$ Lyman break galaxies (LBGs, e.g., Bouwens et al. 2015; Ishigaki et al. 2018; see Stark 2016 for a review) out to $z = 11.1^{+0.08}_{-0.12}$ (Oesch et al. 2016). Furthermore, based on samples of $z \gtrsim 8$ LBGs, Oesch et al. (2018) reported a strong evolution of the ultraviolet (UV) luminosity function by one order of magnitude from $z \sim 10$ to ~ 8, implying a rapid increase of the cosmic star formation rate (SFR) density by an order of magnitude within a very short timescale ($\lesssim 200$ Myr). It is likely that this steep evolution compared to lower z can be explained by the fast build-up of the dark matter halo mass function at $z > 8$ (Oesch et al. 2018).

However, it is still a challenge to characterize the baryonic physics of the $z > 8$ galaxies. One of the major obstacles is that these LBGs are yet to be confirmed through spectroscopy; because the rest-frame UV continuum is typically not sufficiently bright for detection with current instruments, it is often assumed that the Lyα (Lyα) emission line might be the best tool for spectroscopic confirmation. A large amount of 8–10 m telescope time have been invested in Lyα searches for $z > 8$ candidates, but so far this resulted in only a few detections ($z = 8.683$, 8.38, 9.11, Zitrin et al. 2015b; Laporte et al. 2017; Hashimoto et al. 2018c, respectively), likely indicating that the Lyα signal is substantially attenuated by the largely neutral intergalactic medium at this epoch.

Alternative UV indicators such as C III] $\lambda\lambda1907,1909$ Å serve as a workhorse for redshift identification (e.g., Stark et al. 2015a; Zitrin et al. 2015a). These lines, in addition to the rest-frame optical oxygen and nitrogen lines, are also useful for characterizing the metal enrichment of the interstellar medium

(ISM) and stellar components of the galaxies (e.g., Stark et al. 2015a, 2015b, 2017; Mainali et al. 2018). These diagnostic lines will provide unique insights into the physical properties of ionized gas in the $z > 8$ universe when the *James Webb Space Telescope* (*JWST*) comes online, although their use is currently limited to bright galaxies in a certain redshift range, because most of the lines are intrinsically faint and/or are redshifted outside the wavelength range where the atmospheric transmittance is good for ground-based facilities.

With this in mind, Inoue et al. (2014b) investigated the potential use of redshifted nebular emission lines in the rest-frame far-infrared (FIR) in determining spectroscopic redshift of $z \sim 8$ galaxies. The [O III] 88 μm line, which is often observed as the brightest FIR line in local H II regions (e.g., Takami et al. 1987; Kawada et al. 2011), can be used as an instantaneous tracer of massive star formation, because ionization of $O^+ \rightarrow O^{++}$ requires hard ($E > 35.1$ eV) ionizing photons from hot, short-lived O-type stars. Inoue et al. (2014b) predicted the line fluxes from high-z galaxies on the basis of a cosmological hydrodynamic simulation of galaxy formation (Shimizu et al. 2014) by incorporating an [O III] emission line model as a function of metallicity calibrated by *ISO*, *AKARI*, and *Herschel* observations of local galaxies (Brauher et al. 2008; Kawada et al. 2011; Madden et al. 2012, 2013, see also Cormier et al. 2015). Since the metallicity of a typical galaxy with $H_{160} = 26$ mag (AB) reaches $\sim 0.2 Z_\odot$ even at $z \gtrsim 8$, the [O III] line of such galaxies is as bright as 1–5 mJy, which is bright enough to be detected with existing submillimeter facilities, such as the Atacama Large Millimeter/submillimeter Array (ALMA).

Indeed, it is becoming clear that galaxies at $z > 6$ are bright in [O III] 88 μm (Inoue et al. 2016; Carniani et al. 2017; Laporte et al. 2017; Hashimoto et al. 2018a, 2018b, 2018c; Marrone et al. 2018; Walter et al. 2018). The first detection in the EoR has been made for a $z = 7.212$ Lyα emitter, SXDF-NB1006-2 (Inoue et al. 2016), in which only a 2 hr integration of ALMA Band 8 was invested, implying the [O III] line as a promising tool to pin down the spectroscopic redshift even for $z > 8$ galaxies. More recently, two LBGs, A2744_YD4 at $z = 8.38$ (Laporte et al. 2017) and MACS1149-JD1 at $z = 9.1096 \pm 0.0006$ (Hashimoto et al. 2018c), have been confirmed in [O III] at 4.0σ and 7.4σ, respectively. A2744_YD4 was also detected in a 850 μm continuum with $S_{850 \mu m} = 0.1$ mJy, suggesting the presence of a chemically evolved ISM. It should also be noted that MACS1149-JD1 was identified without any prior information for a redshift inferred from a spectral line, demonstrating the [O III] line as the redshift indicator complementing the role of the Lyα and other UV lines.

In addition, the [O III] 88 μm flux places a unique constraint on the stellar and ISM properties, because the [O III] line is extinction-free and sensitive to the electron density, ionization parameter, and gas-phase oxygen abundance of the ionized media, which also depend on global properties such as the SFR and stellar age. Inoue et al. (2016) carried out comprehensive modeling of the UV-to-FIR spectral energy distribution (SED) of SXDF-NB1006-2, in which the [O III] flux and submillimeter continuum upper limits were taken into account. They found this to be a young (<30 Myr) star-forming ($\approx 300 M_\odot$ yr^{-1}) galaxy with a somewhat high best-fitting metallicity of 0.05–1 $Z_\odot$. In contrast, Hashimoto et al. (2018c) revealed that MACS1149-JD1 has a more evolved (290 Myr)

stellar component with a metallicity of 0.2 $Z_\odot$, suggesting a formation redshift of $z_f \approx 15$. The non-detection of a dust continuum in both galaxies suggests low dust-to-metal mass ratios in their ISM (Inoue et al. 2016) compared to the Milky Way's (MW's) value (~ 0.5, e.g., Inoue 2011b), which could indicate that a substantial fraction of ISM metals are not stored in grains.

In this paper, we report the detections of the [O III] 88 μm line and dust continuum in a modestly magnified *Y*-dropout LBG, confirming the spectroscopic redshift to be $z = 8.3118 \pm 0.0003$, i.e., corresponding to an epoch when the age of the universe was only 600 Myr. This is one of the farthest galaxies ever identified spectroscopically by exploiting the brightness of the [O III] line. This paper is organized as follows. Section 2 explains how the target was selected. Section 3 describes the ALMA and VLT/X-shooter observations. Section 4 demonstrates the detection of dust and [O III] emission in MACS0416_Y1. In Section 5, we perform an analysis of the SED to constrain the physical properties of MACS0416_Y1. In Section 6, we discuss the model prediction of the dust mass, whereby we demonstrate that some parameter degeneracies obtained in the SED analysis can be resolved by incorporating a dust mass evolution model. Finally, our conclusions are presented in Section 7.

Throughout this paper, we adopt a concordance cosmology with $\Omega_m = 0.3$, $\Omega_\Lambda = 0.7$ and $H_0 = 70$ km s^{-1} Mpc^{-1}. An angular scale of $1''$ corresponds to the physical scale of 4.7 kpc at $z = 8.312$. A redshift $z = 8.312$ corresponds to an age of the universe of 0.60 Gyr.

2. Target

Among a hundred $z \gtrsim 8$ candidates from treasury *HST* programs (e.g., BoRG, CANDELS, CLASH, HFF, HUDF), we carefully selected a bright ($H_{160} < 26$, AB) galaxy candidate with an accurate photometric redshift (z_{phot}), which is accessible from ALMA ($\delta_{J2000} < +30°$) with good atmospheric transmission. The criteria finally leave MACS0416_Y1 ($H_{160} = 25.92 \pm 0.02$; Infante et al. 2015; Laporte et al. 2015). MACS0416_Y1 lies behind the MACS J0416.1−2403 cluster, one of the *Hubble* Frontier Fields (HFF, Lotz et al. 2017), while the magnification of the LBG is moderate (e.g., magnification factor, $\mu_g = 1.43 \pm 0.04$, Kawamata et al. 2016). Thanks to the deepest *HST* and *Spitzer* photometry, the photo-z is well constrained by six independent studies to be $z_{phot} = 8.478^{+0.062}_{-0.056}$ (Infante et al. 2015), $8.57^{+0.3}_{-0.4}$ (Laporte et al. 2015), 8.42 (Laporte et al. 2016), $8.6^{+0.1}_{-0.1}$ (McLeod et al. 2015), 8.66 (Castellano et al. 2016), and $8.4^{+0.9}_{-0.9}$ (Kawamata et al. 2016). The most likely redshift interval, $8.3 < z < 8.7$, can be covered by four tunings of ALMA Band 7, which offer a wide redshift coverage of $\Delta z \approx 0.72$ for [O III] 88 μm.

3. Observations

3.1. ALMA Observations and Reduction

The ALMA observations were carried out from 2016 October to December and 2017 May to July as a Cycle 4 program (program ID: 2016.1.00117.S). The observation log is given in Table 1. Four different tunings were assigned to cover contiguous frequency range between 340.0 and 366.4 GHz. The local oscillators of the Band 7 receivers were tuned at 347.80, 351.40, 355.00, and 358.60 GHz, and we hereafter denote these tunings as T1, T2, T3, and T4, respectively. The correlator was configured with the frequency-division mode, in
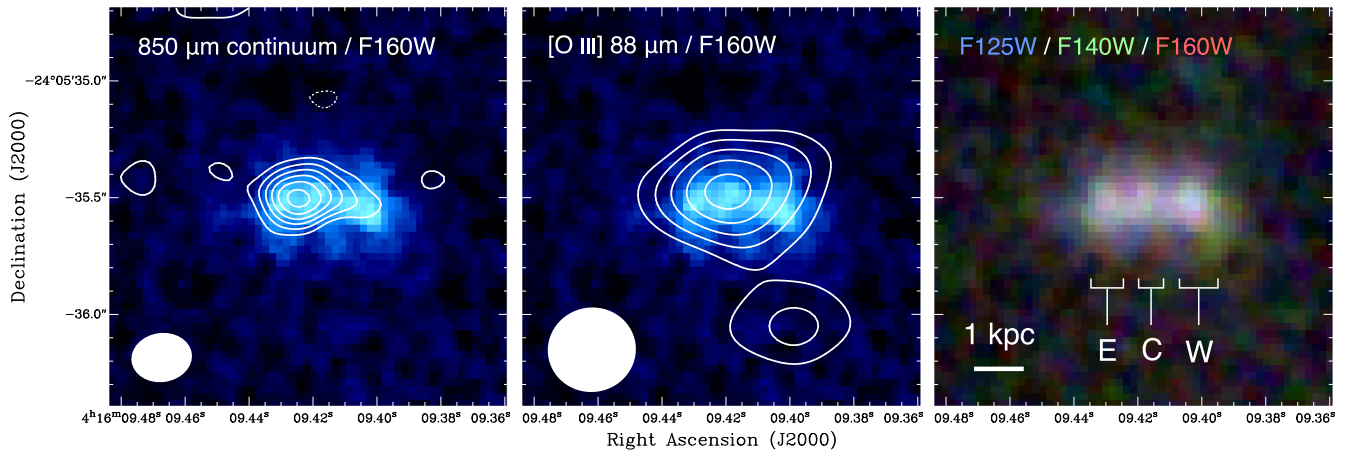
Figure 1. (Left) The ALMA 850 μm continuum image of MACS0416_Y1 (contours) overlaid on the *HST*/WFC3 near-infrared pseudo-color image in the F160W band. The contours are drawn at -2σ, 2σ, 3σ, ..., 7σ, where $\sigma = 10.9\ \mu$Jy beam^{-1}. The negative contour is indicated by the dotted line. The synthesized beam size is indicated in the bottom left corner. (Center) The ALMA [O III] 88 μm integrated intensity image (contours) overlaid on the *HST*/F160W image. The contours are drawn in the same manner as those in the left panel, but $\sigma = 55$ mJy beam^{-1} km s^{-1}. (Right) The false-color *HST*/WFC3 images taken with F160W (red), F140W (green), and F125W (blue) bands. The letters "E," "C" and "W" denote the positions of the eastern, central, and western clumps seen in the rest-frame UV, respectively. The physical scale of 1 kpc on the image plane is indicated by the bar in the bottom left corner.

Table 1
The Parameters of ALMA Observations

UT Start Time[a] (YYYY MM DD hh:mm:ss)	Baseline Lengths (m)	N_{ant}[b]	Center Frequency (GHz)	Integration Time (minutes)	PWV (mm)
2016 Oct 25 05:11:40	19–1399	43	351.40 (T2)	32.76	0.62
2016 Oct 26 09:25:43	19–1184	46	351.40 (T2)	32.76	0.30
2016 Oct 28 09:15:52	19–1124	39	355.00 (T3)	38.30	0.35
2016 Oct 29 07:10:42	19–1124	41	347.80 (T1)	33.77	1.27
2016 Oct 30 07:36:05	19–1124	39	355.00 (T3)	38.30	0.93
2016 Oct 30 08:55:42	19–1124	40	347.80 (T1)	33.77	0.78
2016 Nov 2 04:23:49	19–1124	40	358.60 (T4)	30.23	0.64
2016 Nov 2 05:31:01	19–1124	40	358.60 (T4)	30.23	0.97
2016 Dec 17 05:37:41	15–460	44	347.80 (T1)	33.77	0.90
2016 Dec 18 05:21:55	15–492	47	347.80 (T1)	33.77	1.29
2017 Apr 28 21:51:39	15–460	39	355.00 (T3)	38.30	0.72
2017 Jul 3 12:28:53	21–2647	40	358.60 (T4)	30.23	0.24
2017 Jul 4 12:40:06	21–2647	40	358.60 (T4)	30.23	0.41

Notes.
[a] At integration start.
[b] The number of antenna elements.

which the four spectral windows (SPWs) cover 7.5 GHz with respect to the central frequencies with a channel spacing of 7.8125 MHz. The phase tracking center was set to the LBG position, $(\alpha_{J2000}, \delta_{J2000}) = (04^{h}16^{m}09\overset{s}{.}4010, -24°05'35\overset{''}{.}470)$, which was determined by the *HST* observations (Infante et al. 2015; Laporte et al. 2015). The on-source time was 436 minutes in total. Two quasars, J0348−2749 and J0453−2807, were used for complex gain calibration. J0522−3627 was used for bandpass calibration. Flux was scaled using J0522−3627 (for the tunings T2 and T3, $S_{850\ \mu m} \simeq 3$–4 Jy) and J0334−4008 (for the tunings T1 and T4, $S_{850\ \mu m} \simeq 0.3$ Jy), yielding an absolute accuracy better than 10%.

The calibration and flagging were made using a standard pipeline running on CASA (McMullin et al. 2007) version 4.7.2, while manual flagging was needed for some outlier antennas. Four tuning data are combined to make the continuum image using the CASA task, `clean`, with the natural weighting. Note that spectral channels where the [O III] line is detected were not

used for continuum imaging. The resulting synthesized beam size in FWHM is $0\overset{''}{.}26 \times 0\overset{''}{.}21$ (position angle PA $= -82°$). Synthesized beam deconvolution is made down to 2σ.

Each tuning data set was also imaged to produce a cube with a frequency resolution of 31.25 MHz ($\approx$26 km s^{-1}) to search for the [O III] line. As the data sets were obtained in different array configurations and some SPWs with long baselines may resolve out the emission, we optimally taper the image with a $0\overset{''}{.}35$ Gaussian kernel to maximize the signal-to-noise ratio (S/N) of the emission. The resulting beam size and rms noise level measured at 364 GHz are $0\overset{''}{.}38 \times 0\overset{''}{.}36$ (PA $= -79°$) and $\sigma = 0.5$ mJy beam^{-1}, respectively (Figures 1 and 3).

3.2. ALMA and Hubble Astrometry

The position of the LBG was originally determined by the HFF *HST* images, which are aligned to the existing CLASH catalogs (Postman et al. 2012); the CLASH astrometry was based on Subaru's Suprime-Cam catalogs which are registered

Table 2
The Observed Quantities of MACS0416_Y1

| $S_{850\,\mu m}$ (μJy) | FWHM[a] (arcsec) | $T_{dust} = 40$ K | | $T_{dust} = 50$ K | | $F_{[O\,III]}$ (Jy km s^{-1}) | $\Delta V_{[O\,III]}$ (km s^{-1}) | z | $L_{[O\,III]}$[b] ($10^9 L_\odot$) |
		L_{IR}[b] ($10^{11}L_\odot$)	M_{dust}[b] ($10^6 M_\odot$)	L_{IR}[b] ($10^{11}L_\odot$)	M_{dust}[b] ($10^6 M_\odot$)				
137 ± 26	$0\rlap{.}''36 \times 0\rlap{.}''10$	1.1 ± 0.2	8.2 ± 1.6	1.7 ± 0.3	3.6 ± 0.7	0.66 ± 0.16	141 ± 21	8.3118 ± 0.0003	1.2 ± 0.3

Notes. The error represents the 68% confidence interval.
[a] The beam-deconvolved source size measured for the continuum image.
[b] The value is corrected for a lensing magnification of $\mu_g = 1.43 \pm 0.04$ (Kawamata et al. 2016), while the error bar does not include the uncertainty in μ_g. The IR luminosity is derived from a modified blackbody defined in the range of 8–1000 μm. Note that no Wien correction is applied when the IR luminosity is derived. The extra heating from the cosmic microwave background is taken into account in deriving the IR luminosity and dust mass according to the formulation by da Cunha et al. (2013). The dust emissivity is assumed such that $\kappa_d(\nu) = \kappa_d(850\,\mu m)(\nu/\nu_0)^\beta$, where $\nu_0 = 353$ GHz, $\kappa_d(850\,\mu m) = 0.15$ m^2 kg^{-1} (e.g., Weingartner & Draine 2001; Dunne et al. 2003) and $\beta = 1.5$ are the dust absorption coefficient and the emissivity index, respectively.

onto the Two-Micron All Sky Survey (2MASS) frame. We find, however, that the optical-to-NIR astrometry does not fully match the International Celestial Reference System (ICRS) on which ALMA relies. In order to correct the astrometry of the *HST* images, we use four positions of objects (3 stars and 1 cluster elliptical) accurately measured in the *Gaia* first data release (DR1) catalog (Gaia Collaboration et al. 2016a, 2016b). We also compare the positions of the three quasars used as ALMA phase calibrators, J0348−2749, J0453−2807, and J0522−3627, which are determined by the *Gaia* DR1 catalog and by phase solutions from our ALMA calibration. We find that the relative offsets between the ALMA and *Gaia* coordinates are typically <10 mas. All of the *HST* images are corrected for astrometry on the basis of the *Gaia* coordinates using the IRAF (Tody 1993) task, ccsetwcs, confirming those two frames coincide with each other down to the accuracy of $\lesssim$30 mas. The resulting centroid of the LBG in the ICRS coordinate is at $(\alpha_{ICRS}, \delta_{ICRS}) = (04^h16^m09\rlap{.}^s415, -24°05'35\rlap{.}''54)$. We hereafter use this coordinate as the formal position of MACS0416_Y1.

3.3. X-shooter Observations and Reduction

To verify the redshift of MACS0416_Y1 we aimed to detect the redshifted UV emission lines from either Lyα, C IV $\lambda\lambda$1548, 1550 Å, C III] $\lambda\lambda$1907,1909 Å, or O III] $\lambda\lambda$1661, 1666 Å.

We observed MACS0416_Y1 with VLT/X-shooter (Vernet et al. 2011) for a total of 10 hr on target. The observations were carried out at 10 different nights between 2017 December 8 and 2018 January 21 (Program ID: 0100.A-0529(A), PI: Zackrisson). A blind offset from a neighboring star was used to place the slit on the galaxy using the coordinates from *HST* images. A $1\rlap{.}''2$ wide slit was chosen at optical and near-IR wavelengths in order to capture the rest-frame UV emission from the galaxy, and the slit was aligned along the parallactic angles (between 95° and 100° east of north). The observations were carried out in an ABBA nodding mode pattern with 4×900 s integrations. During the observations, the sky transmission was clear or photometric and the seeing varied between $0\rlap{.}''4$ and $0\rlap{.}''8$, yielding the best possible conditions for detecting faint emission lines.

The data were reduced with ESOREX scripts (Modigliani et al. 2010) using adjacent positions in the nodding sequence for sky background subtraction. Corrections for telluric absorption lines were applied from models with MOLECFIT (Kausch et al. 2015) applied to observations of hot stars following the science integrations. Errors were propagated

throughout the data processing steps. Since the seeing FWHM was smaller than the slit widths, we measured the spectral resolutions from telluric absorption lines, yielding effectively $R = 5600$ in the near-IR spectra. Observations of spectro-photometric standard stars on each of the 10 nights were used to flux calibrate each spectrum before they were co-added.

4. Results

4.1. Detection of 850 μm Dust Continuum

We detect 850 μm (i.e., rest-frame 90 μm) continuum emission at the position of MACS0416_Y1 as shown in Figure 1 (left). The peak ICRS position is $(\alpha_{ICRS}, \delta_{ICRS}) = (04^h16^m09\rlap{.}^s423 \pm 0\rlap{.}^s002, -24°05'35\rlap{.}''50 \pm 0\rlap{.}''01)$. The rms noise level after combining all of the SPWs is $\sigma = 10.9\,\mu$Jy beam^{-1}, yielding a significance of 7.6σ on the resulting image. The flux density and the image component size deconvolved with the synthesized beam are measured using a CASA task imfit with an assumption that the sources are two-dimensional Gaussians and are found to be $S_{850\,\mu m} = 137 \pm 26\,\mu$Jy and $(0\rlap{.}''36 \pm 0\rlap{.}''09) \times (0\rlap{.}''10 \pm 0\rlap{.}''05)$ in FWHM (PA = +84°), respectively. This elongation is not likely due to the cluster magnification but rather the intrinsic shape of the LBG, because its elongation does not align with the lensing shear direction. The overall spatial distribution of the 850 μm continuum is similar to that of the rest-frame UV emission, while the bulk of dust emission is likely to be associated with the eastern "E" knot (or a gap between the "E" and central "C" knots) seen in the *HST*/WFC3 image (Figure 1 right).

We also retrieve a previous 1.14 mm imaging result obtained for the MACS J0416.1−2403 cluster (González-López et al. 2017). No 1.14 mm emission is found with the 2σ upper limit of 116 μJy. This places an upper limit on the spectral index between 1.14 mm and 850 μm to be $\alpha > 0.6$ (2σ), where α is defined such that $S_\nu \propto \nu^\alpha$. Despite a relatively weak constraint, this could rule out a low-z interloper with non-thermal emission from an active galactic nucleus, where $\alpha \sim -0.7$ is expected. Instead, the spectral index is consistent with dust continuum emission with a temperature of $\gtrsim$30 K. The observed flux density of $S_{850\,\mu m} = 137 \pm 26\,\mu$Jy corresponds to a de-lensed total IR luminosity of $L_{IR} = (1.7 \pm 0.3) \times 10^{11}L_\odot$ $[(1.1 \pm 0.2) \times 10^{11}L_\odot]$ and a dust mass of $M_{dust} = (3.6 \pm 0.7) \times 10^6 M_\odot$ $[8.2 \pm 1.6) \times 10^6 M_\odot]$ when assuming a dust temperature of $T_{dust} = 50$ K (40 K) and a magnification factor of $\mu_g = 1.43 \pm 0.04$ (see Table 2 for more details).
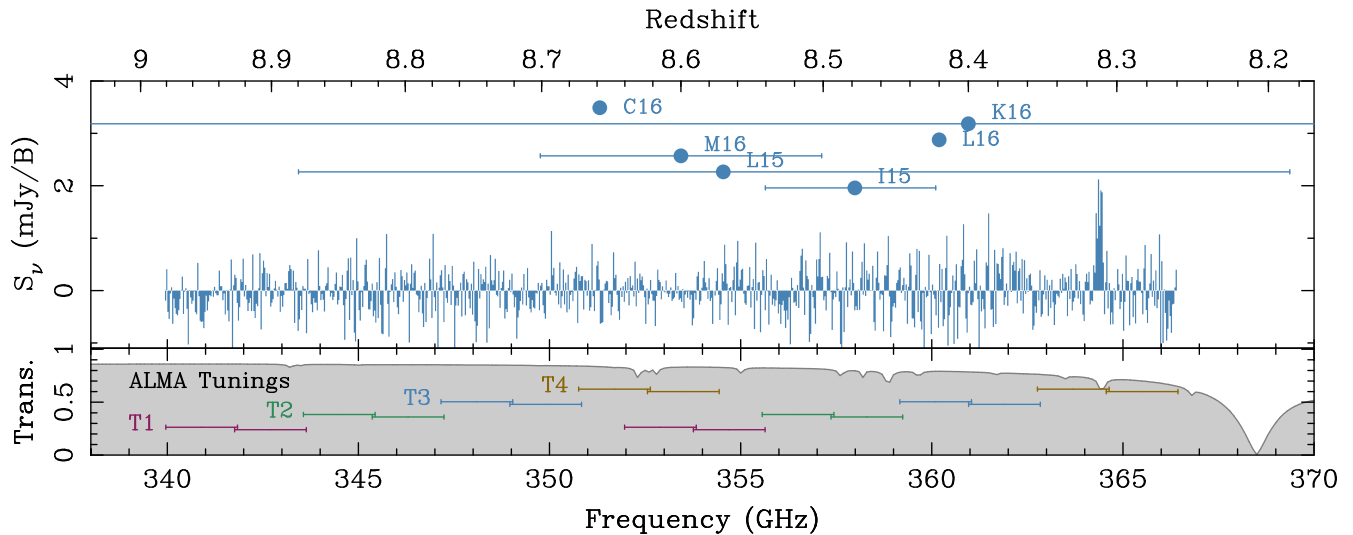
Figure 2. The full ALMA spectrum produced by combining four independent tunings T1–T4. The spectrum is continuum-subtracted. The blue dots with error bars represent the photometric redshifts with a 68% confidence interval measured by six independent studies (Infante et al. 2015, denoted as I15; Laporte et al. 2015, L15; McLeod et al. 2015, M15; Laporte et al. 2016, L16; Kawamata et al. 2016, K16; and Castellano et al. 2016, C16). The lower panel shows the atmospheric transmission under a precipitable water vapor (PWV) of 0.9 mm, a moderate condition at the ALMA site. The horizontal bars show the coverage of the four tunings, T1–T4, each of which has four spectral windows.

4.2. Blind Detection of [O III] 88 μm

At the position of the dust emission, we detect an emission line feature at 364.377 ± 0.012 GHz, strongly suggesting a [O III] 88 μm emission line at $z = 8.3118 \pm 0.0003$ (Figure 2). This redshift is slightly lower than but consistent with the photometric redshifts. This is a rather common feature seen in LBGs in the reionization era (e.g., MACS1149-JD1, Zheng et al. 2017; Hashimoto et al. 2018c); the slight offset is likely due to the fact that the largely neutral interstellar/intergalactic medium attenuates the edge of the Lyman break and makes the photo-z estimates higher. Figure 1 (center) shows the integrated intensity image where the [O III] line is detected at 6.3σ. The intensity peak is associated with the "E"–"C" clumps seen in the HST/F160W image (Figure 1 right). The apparent flux is $F_{[O III]} = 0.66 \pm 0.16$ Jy km s^{-1}, corresponding to the de-lensed luminosity of $L_{[O III]} = (1.2 \pm 0.3) \times 10^9 L_\odot$. The image may barely be resolved and has a beam-deconvolved size of $\sim 0\overset{''}{.}5 \times 0\overset{''}{.}3$ (PA = 89°) despite a large uncertainty. The line width is estimated by a Gaussian fit (Figure 3) and is found to be $\Delta V_{[O III]} = 141 \pm 21$ km s^{-1} in FWHM, which is consistent with those predicted for dark halos hosting a bright ($H_{160} \sim 26$) galaxy at $z \sim 8$ in a cosmological hydrodynamic simulation (Inoue et al. 2014b; Shimizu et al. 2014). The line width is also similar to those found in SXDF-NB1006-2 at $z = 7.212$ ($\Delta V_{[O III]} \approx 80$ km s^{-1}, Inoue et al. 2016) and MACS1149-JD1 at $z = 9.110$ (154 ± 39 km s^{-1}, Hashimoto et al. 2018c), but broader than that of A2744-YD4 ($\Delta V_{[O III]} \simeq 43$ km s^{-1}, Laporte et al. 2017). The observed quantities are summarized in Table 2.

Figure 4 shows the [O III]-to-IR luminosity ratio, $L_{[O III]}/L_{IR}$,[19] found in local and high-z galaxies as a function of L_{IR}. It is known that the $L_{[O III]}/L_{IR}$ ratios exhibit a possible weak anti-correlation with L_{IR} as suggested by earlier studies of local galaxies (De Looze et al. 2014; Cormier et al. 2015;
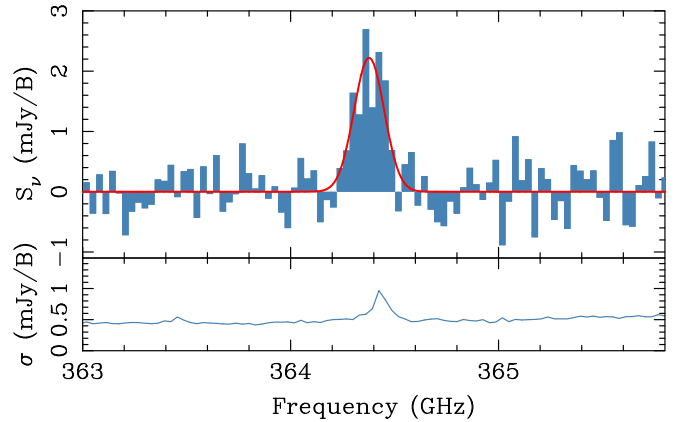

Figure 3. Continuum-subtracted spectrum showing the [O III] line (top) with the best-fitting Gaussian function (red curve). The lower panel shows the 1σ noise level, where an atmospheric absorption line is seen close to the [O III] line.

Díaz-Santos et al. 2017). The $L_{[O III]}/L_{IR}$ of MACS0416_Y1 is estimated to be $L_{[O III]}/L_{IR} \approx 7 \times 10^{-3}$ and is comparable to those found in the *Herschel* Dwarf Galaxy Survey ($L_{[O III]}/L_{IR} = 5.0^{+16.6}_{-1.5} \times 10^{-3}$, Cormier et al. 2015). The ratio is as high as those found for $z = 7$–9 UV-selected galaxies, such as SXDF-NB1006-2 ($L_{[O III]}/L_{IR} > 1.3 \times 10^{-2}$, Inoue et al. 2016), MACS1149-JD1 ($>7 \times 10^{-3}$, Hashimoto et al. 2018c), B14-65666 (4.6×10^{-3}, Hashimoto et al. 2018a), BDF-3299 ($>2 \times 10^{-3}$, Carniani et al. 2017), and A2744_YD4 at $z = 8.38$ ($\sim 1 \times 10^{-3}$, Laporte et al. 2017), although SXDF-NB1006-2 and MACS1149-JD1 may have much higher values. The ratio of MACS0416_Y1, however, exhibits a sharp contrast to those found in local spirals, ultra-luminous IR galaxies (Herrera-Camus et al. 2018a, 2018b; see the gray open squares in Figure 4), $z \sim 2$–7 submillimeter galaxies ($\simeq 1 \times 10^{-3}$ or less, Ferkinhoff et al. 2010; Valtchanov et al. 2011; Marrone et al. 2018; Vishwas et al. 2018), and an IR-luminous quasar APM 08279+5255 (3×10^{-4}, Ferkinhoff et al. 2010).

---

[19] Here, we assume $T_{dust} = 50$ K for the L_{IR} of $z > 7$ galaxies for which T_{dust} is unknown. The $L_{[O III]}/L_{IR}$ ratio increases by a factor of 1.5 if assuming $T_{dust} = 40$ K.
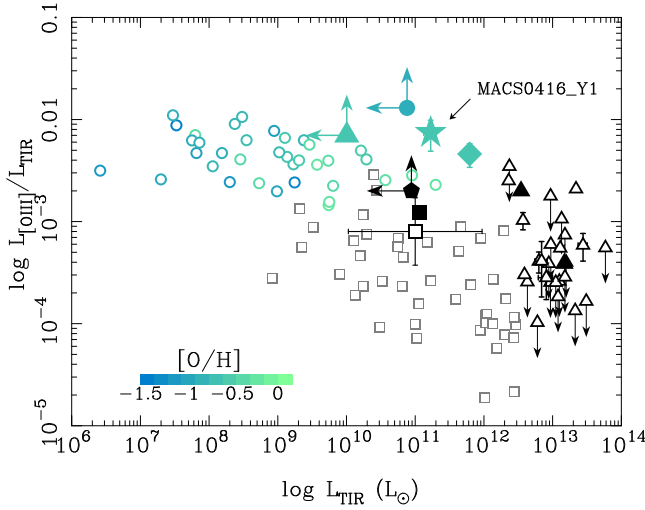
Figure 4. [O III]-to-IR luminosity ratio as a function of IR luminosity. The filled symbols represent the galaxies at $z \gtrsim 7$, i.e., MACS0416_Y1 (five-pointed star), SXDF-NB1006-2 (filled circle with two arrows, Inoue et al. 2016), BDF-3299 (filled pentagon, Maiolino et al. 2015; Carniani et al. 2017), A2744_YD4 (filled square, Laporte et al. 2017), MACS1149-JD1 (filled triangle with two arrows, Hashimoto et al. 2018c), B14-65666 (filled diamond, Hashimoto et al. 2018a), and SPT0311−58 E/W (filled triangles, Marrone et al. 2018). The open symbols are lower-z galaxies, local dwarfs (open circles, Madden et al. 2013; Cormier et al. 2015), the SHINING samples of local star-forming galaxies from normal spirals to ultra-luminous IR galaxies (small gray open squares, Herrera-Camus et al. 2018a, 2018b), the median of local spirals (large black open square with the error bar representing 1.5 times the median absolute deviation, Brauher et al. 2008), and $z \sim 2$–4 dusty star-forming galaxies (open triangles, Ferkinhoff et al. 2010; Ivison et al. 2010; Valtchanov et al. 2011; Vishwas et al. 2018). All of the $z > 7$ galaxies, except for SPT0311 −58 E/W, are assumed to have a dust temperature of $T_{\mathrm{dust}} = 50$ K; note that L_{IR} decreases by a factor of 0.7 if assuming $T_{\mathrm{dust}} = 40$ K. The IR luminosities are corrected for magnification, if any. The blue-to-green color code shown for MACS0416_Y1, SXDF-NB1006-2, MACS1149-JD1, B14-65666, and local dwarfs indicates the best-fitting oxygen abundances.

4.3. UV Emission Line Detection Limits

The final two-dimensional spectrum from X-shooter covering near-IR wavelengths at 1–2.4 μm was inspected for emission lines. At the redshift of [O III] 88 μm from ALMA ($z = 8.3118$) no rest-frame UV emission lines were detected. Furthermore, no emission lines could be visually identified at other wavelengths. To determine detection limits, we added artificial emission lines with varying FWHMs at the expected wavelengths and extracted one-dimensional spectra and their associated error spectra. To enhance the S/N detection limit, we binned the data in the spectral dimension by varying factors between 3 and 7 pixels (see Watson et al. 2015). To confidently detect an emission line we require a S/N = 5 detection. Table 3 summarizes the detection limits for lines with FWHM ranging from 50 to 150 km s^{-1} for the brighter of the doublet lines. Since Lyα is a resonance line, we also compute the detection limit for a larger width of 250 km s^{-1}. Typical limits are of the order of a few times 10^{-18} erg s^{-1} cm^{-2}. The reported limits have not been corrected for lens magnifications.

5. Physical Properties of MACS0416_Y1

The ALMA observations clearly show that MACS0416_Y1 has a substantial amount of dust that exhibits a similar spatial distribution to the rest-frame UV emission on a ~ 1 kpc scale. This is somewhat surprising because the UV slope is blue ($\beta_{\mathrm{UV}} \approx -2$) and earlier studies have actually suggested small

Table 3
The 5σ Detection Limits of UV Emission Lines in X-shooter Data Assuming Redshift $z = 8.3118$

Lines	5σ Detection Limits		
	250 km s^{-1}	150 km s^{-1}	50 km s^{-1}
Lyα	<8.0	<5.0	<3.0
C IV $\lambda\lambda$1548, 1550 Å	...	<4.0	<1.8
O III] λ1666 Å[a]	...	<5.2	<3.0
C III] λ1907 Å[a]	...	<6.0	<2.4

Note. The detection limits are measured for line widths (FWHM) of 250, 150, and 50 km s^{-1}. The limits are not corrected for magnification. The flux limits are in units of 10^{-18} erg s^{-1} cm^{-2}.
[a] The detection limit for the brighter of the doublet lines.

Table 4
The Photometric Data of MACS0416_Y1

Instrument	Wavelength (μm)	AB Magnitude[a] (mag)	Flux Density[b]	
			Value	Unit
HST/F435W	0.431	>30.07	<3.40	nJy
HST/F606W	0.589	>30.40	<2.51	nJy
HST/F814W	0.811	>30.32	<2.70	nJy
HST/F105W	1.05	>29.83	<4.25	nJy
HST/F125W	1.25	26.41 ± 0.07	99^{+7}_{-6}	nJy
HST/F140W	1.40	26.08 ± 0.05	134^{+6}_{-6}	nJy
HST/F160W	1.55	26.04 ± 0.05	139^{+7}_{-6}	nJy
VLT/HAWK-I (K_S)	2.152	26.37 ± 0.39	103^{+44}_{-31}	nJy
Spitzer/IRAC (ch1)	3.6	>25.32	<270	nJy
Spitzer/IRAC (ch2)	4.5	24.94 ± 0.29	384^{+117}_{-90}	nJy
ALMA/Band 7	850	...	137 ± 26	μJy
ALMA/Band 6	1140	...	<116	μJy

Notes. All values are not corrected for cluster lensing magnification.
[a] The error bars represent the 68% confidence interval. The lower limit is given at 2σ, where σ is obtained by randomly measuring the sky with PSF diameter apertures. All of the photometry values were obtained in this work; see Laporte et al. (2015) (*HST* and *Spitzer*) and Brammer et al. (2016) (VLT/HAWK-I) for original imaging data.
[b] The error bars represent the 68% confidence interval. The upper limit is given at 2σ.

dust extinction with $A_V \lesssim 0.4$ (e.g., Laporte et al. 2015). Furthermore, the *Spitzer*/IRAC photometry shows a red color in the rest-frame optical ([3.6]–[4.5] > 0.38; see Table 4). The attribution includes (i) the stellar population with the Balmer break at $\lambda_{\mathrm{obs}} \approx 3.7$ μm and (ii) a substantial contribution of the optical [O III] $\lambda\lambda$4959, 5007 Å lines to the 4.5 μm band (e.g., Labbé et al. 2013; Smit et al. 2015). The former case is expected for a relatively evolved stellar component, while the latter requires a much younger stellar population where OB stars are dominant in luminosity.

5.1. SED Model

Here, we characterize the SED to investigate the physical properties of MACS0416_Y1 by template fits where stellar populations, UV-to-FIR nebular emission, and dust thermal emission are taken into account. We use the photometric data of the 850 μm continuum and [O III] line in addition to the rest-frame UV-to-optical bands (Table 4) to model the SED of MACS0416_Y1. The model is based on the prescription
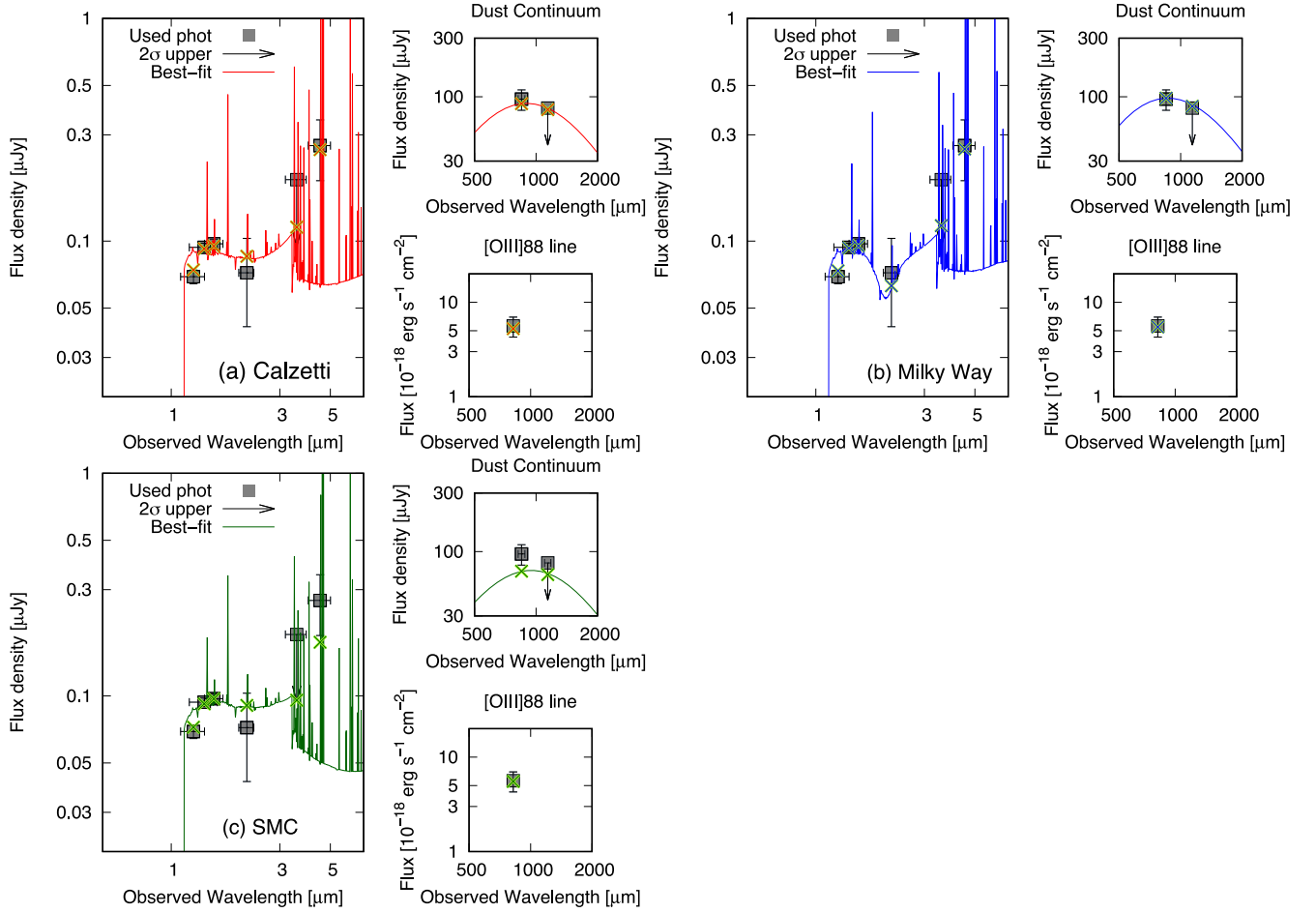
Figure 5. Best-fitting spectral energy distributions (SEDs) for three dust extinction laws. (a) The SEDs modeled with the Calzetti dust extinction law. The filled and open squares represent the observed photometric data points, while the photometric data at <1 μm are not used for SED fits. Those of the rest-frame FIR constraints are shown in the small panels. The solid curve is the best-fitting SEDs. The crosses are flux densities (or flux for the [O III] 88 μm line) predicted from the model. (b) The same plot, but the Milky Way dust extinction law is used. The overall trend is the same as the Calzetti case, while the K_s band decrement is well explained by the 2175 Å feature of the extinction law. (c) The same plot, but the SMC extinction law is used.

presented by Mawatari et al. ([2016](#)) and K. Mawatari et al. (2019 in preparation),[20] where the emission components of a stellar continuum (Bruzual & Charlot [2003](#)), rest-frame UV-to-optical nebular lines (Inoue [2011a](#)), and dust continuum (Rieke et al. [2009](#)) are accounted for. In addition, we take into account the [O III] 88 μm line (Inoue et al. [2014b](#)) and nebular continuum in the UV-to-optical wavelengths (Inoue [2011a](#)). We use the stellar population synthesis model from Bruzual & Charlot ([2003](#)) with the Chabrier initial mass function (IMF) defined in the range of 0.1–100 $M_\odot$ (Chabrier [2003](#)). We assume exponentially declining and rising SFRs expressed as

$$\mathrm{SFR}(\tau_{\mathrm{age}}) = \frac{1}{|\tau_{\mathrm{SFH}}|} \exp\left(-\frac{\tau_{\mathrm{age}}}{\tau_{\mathrm{SFH}}}\right), \qquad (1)$$

where τ_{age} is the age of the galaxy that ranges from 0.1 Myr to the age of the universe at $z = 8.312$, and τ_{SFH} is the e-folding timescale of SFR and is set to ± 0.01, ± 0.1, ± 1, and ± 10 Gyr. The positive and negative timescales represent declining and rising SFRs, respectively. For rising SFRs (i.e., $\tau_{\mathrm{SFH}} < 0$), we just fix $\mathrm{SFR}(\tau_{\mathrm{age}}) = \frac{1}{|\tau_{\mathrm{SFH}}|} \exp(10)$ at $\tau_{\mathrm{age}} > 10\tau_{\mathrm{SFH}}$ to

avoid SFRs diverging. We also explore five metallicity values of $Z = 0.0001$, 0.0004, 0.004, 0.008, and 0.02 (ranging 1/200–1 $Z_\odot$). Three extinction laws from Calzetti et al. ([2000](#)), Small Magellanic Cloud (SMC, Prevot et al. [1984](#); Bouchet et al. [1985](#)) and MW (Fitzpatrick & Massa [1986](#), who fit data obtained by Seaton [1979](#)) are employed in the range of $A_V = 0$–5 to account for dust extinction.

The nebular continuum and lines arising from ionized gas are modeled by relating the Lyman continuum (LyC) photon rate, metallicity, and nebular emissivity. The ionizing photon rate is determined for each grid of stellar age and metallicity in the stellar population synthesis model. Following Inoue ([2011a](#)), we derive the electron temperature, the nebular continuum emissivity for a unit LyC photon rate, and the nebular line emissivities for a unit Hβ flux, as a function of metallicity. Hβ flux is derived by assuming the case B recombination. The escape fraction of LyC photons, f_{esc}, is treated as a free parameter, while that of Lyα photons is fixed to 1. We accordingly attenuate the flux densities at $\lambda_{\mathrm{rest}} < 912$ Å by a factor of f_{esc}. We ignored LyC absorption by dust for simplicity. The intergalactic H I transmission model of Inoue et al. ([2014a](#)) is also adopted with an extrapolation from $z < 6$ to $z = 8.3$. This simply diminishes the flux below the Lyα wavelength including the Lyα emission line. For

---

Table 5
Best-fitting Parameters of the Rest-frame Ultraviolet to Far-infrared Spectral
Energy Distribution of MACS0416_Y1

Items	Extinction Law		
	Calzetti	MW	SMC
χ^2	7.1	6.8	8.4
Degree of freedom	3	3	3
Dust attenuation A_V (mag)	$0.50^{+0.09}_{-0.13}$	$0.50^{+0.08}_{-0.16}$	$0.20^{+0.10}_{-0.08}$
Age $\tau_{\rm age}$ (Myr)	$3.5^{+0.7}_{-2.3}$	$4.2^{+0.3}_{-3.0}$	$2.0^{+1.6}_{-0.6}$
SFH $\tau_{\rm SFH}^{-1}$ (Gyr^{-1})[a]	100^{+0}_{-200}	-10^{+110}_{-90}	100^{+0}_{-200}
Metallicity Z ($Z_\odot$)	$0.20^{+0.16}_{-0.18}$	$0.20^{+0.17}_{-0.18}$	$0.20^{+0.54}_{-0.17}$
LyC escape fraction $f_{\rm esc}$	$0.00^{+0.19}_{-0.00}$	$0.00^{+0.14}_{-0.00}$	$0.40^{+0.21}_{-0.40}$
Stellar mass $M_{\rm star}$ ($10^8 M_\odot$)[b]	$2.4^{+0.7}_{-0.1}$	$2.4^{+0.6}_{-0.3}$	$2.2^{+0.5}_{-0.2}$
SFR ($M_\odot$ yr^{-1})[b]	$57^{+175}_{-0.2}$	60^{+168}_{-2}	100^{+56}_{-33}
$L_{\rm IR}$ ($10^{11} L_\odot$)[b]	$1.5^{+0.2}_{-0.3}$	$1.6^{+0.1}_{-0.4}$	$1.2^{+0.5}_{-0.2}$

Notes. The error bars represent the 68% confidence interval estimated from probability distribution functions (PDFs) on the basis of a Monte Carlo technique following the prescription presented by Hashimoto et al. (2018c). The probability distributions for the fitting parameters are presented in the Appendix.
[a] $\tau_{\rm SFH}^{-1} = 0$, $\tau_{\rm SFH}^{-1} > 0$, and $\tau_{\rm SFH}^{-1} < 0$ represent constant, exponentially declining and rising star formation histories as defined in Equation (1).
[b] The value is corrected for lensing magnification with $\mu_{\rm g} = 1.43 \pm 0.04$ (Kawamata et al. 2016), while the error bar does not include the uncertainty in $\mu_{\rm g}$.

[O III] 88 μm, we use the prescription of Inoue et al. (2014b), where the [O III] emissivity for a unit SFR (i.e., $L_{\rm [O\,III]}$/SFR) is assumed to be modeled as a function of metallicity. This ($L_{\rm [O\,III]}$/SFR)-to-metallicity relation is calibrated by *ISO*, *Herschel*, and *AKARI* observations of local dwarfs and spirals (Brauher et al. 2008; Kawada et al. 2011; Madden et al. 2013; De Looze et al. 2014; Cormier et al. 2015). We do not use the X-shooter upper limits on the individual UV line fluxes for the model constraint, because the UV line intensities are sensitive to physical properties of ionized media, such as electron density and ionization parameter (e.g., Inoue 2011a), which could induce large uncertainties in the UV nebular line emissivities.

We compute the 5–1000 μm luminosity $L_{\rm IR}$ for each stellar model grid and extinction by assuming that $L_{\rm IR}$ is equivalent to the luminosity of stellar and nebular emission at 0.01–2.2 μm absorbed by dust. We then assign an IR-to-millimeter SED for each stellar component and extinction on the basis of $L_{\rm IR}$. The shapes of the SEDs were determined for local luminous infrared galaxies and modeled as a function of $L_{\rm IR}$ (Rieke et al. 2009).

5.2. Results

The results are shown in Figure 5 and Table 5.[21] One of the important outcomes is that there exist solutions that reasonably explain the large amount of dust coexisting with the young stellar components. Regardless of the extinction law, the SED fits favor a young, high-SFR solution, where large equivalent widths of the enhanced [O III] $\lambda\lambda$4959, 5007 Å and Hβ lines contribute to the [3.6]–[4.5] color. The SFR and age are estimated to be $\approx 60 M_\odot$ yr^{-1} and ≈ 4 Myr, respectively, suggesting that MACS0416_Y1 is at the onset of a starburst phase. The carbonaceous absorption feature of the MW extinction law at $\lambda_{\rm rest} \approx 2175$ Å can explain the blue $H - K_S$ color, although the predicted flat UV spectrum assuming the

---

[21] See also the Appendix for the probability distributions for the SED parameters.

Calzetti or SMC law is not ruled out because of a large uncertainty in K_S band photometry. The best-fitting metallicity already reaches $Z \approx 0.2 Z_\odot$ at $z = 8.3$ despite a large uncertainty, suggesting rapid enrichment of heavy elements in the middle of the reionization era.

This does not, however, explain how the galaxy has *obtained* the large amount of dust, even though the SED model explains the energy budget self-consistently if assuming that the dust *pre-exists*. The dust-to-stellar mass ratio inferred from the SED fits is $M_{\rm dust}/M_{\rm star} \sim 1 \times 10^{-2}$. This is 1–2 orders of magnitude higher compared to the median value obtained for 29 local dwarf galaxies from the *Herschel* Dwarf Galaxy Survey (Madden et al. 2013; Rémy-Ruyer et al. 2015), which is $M_{\rm dust}/M_{\rm star} = 2^{+12}_{-1.8} \times 10^{-4}$, where the error bar represents the 90 percentile. The ratio would even be an order of magnitude higher than those of dusty star-forming galaxies (e.g., da Cunha et al. 2010; Smith et al. 2012; Clark et al. 2015; De Vis et al. 2017); for instance, a median of $M_{\rm dust}/M_{\rm star} = 4.2 \times 10^{-3}$ is observed for 1402 250 μm selected normal star-forming galaxies at $z < 0.5$ from the *Herschel*-ATLAS survey (Smith et al. 2012). These facts suggest that the stellar mass of MACS0416_Y1 could significantly be underestimated if only ongoing star formation is taken into account, implying the presence of a more massive, evolved stellar population. Note that a very high dust temperature (e.g., $T_{\rm dust} \sim 100$ K) could only reduce the dust mass by a factor of ~ 5 and does not fully explain the high $M_{\rm dust}/M_{\rm star}$ ratio. The evolved stellar component as a result of past star formation activity is also expected as the origin of the dust mass, which will be discussed in the following section.

6. Discussions

The stellar SED analysis presented in Section 5 has highlighted an extremely young, star-forming stellar component. The solution also explains the IR luminosity if the dust mass pre-exists, while it needs to be discussed whether the large dust mass can be attained in the very short duration ($\sim 10^{-3}$ Gyr). The high $M_{\rm dust}/M_{\rm star}$ ratio implies the presence of a more massive, evolved stellar component that does not contribute significantly to the rest-frame UV. However, it is not clear how the evolved component plays a role in dust mass assembly. In this section, we discuss how our current understanding of dust formation and evolution reproduces the dust mass observed in MACS0416_Y1.

6.1. Dust Mass Evolution Model

In the past decade, substantial amounts of dust ranging from 10^6 to $10^8 M_\odot$ have been identified in $z > 7$ galaxies and quasars (Venemans et al. 2012, 2017; Watson et al. 2015; Laporte et al. 2017; Hashimoto et al. 2018a), which poses a challenge to the current theory of dust formation (Michałowski 2015). In the local universe, the origins of dust grains are the stellar winds of asymptotic giant branch (AGB) stars and ejecta of type II supernovae (SNe II), although the accretion of gas-phase metal onto grains should play a dominant role. In fact, grain growth in dense, metal-polluted ISM is considered to be a major contributor to the dust mass in the MW (e.g., Dwek 1998; Zhukovska et al. 2008; Draine 2009). Furthermore, processes in diffuse gas, such as dust destruction by SN shocks and shattering by grain collisions, control the effective dust yield per SN and the size distribution (Draine & Salpeter 1979).
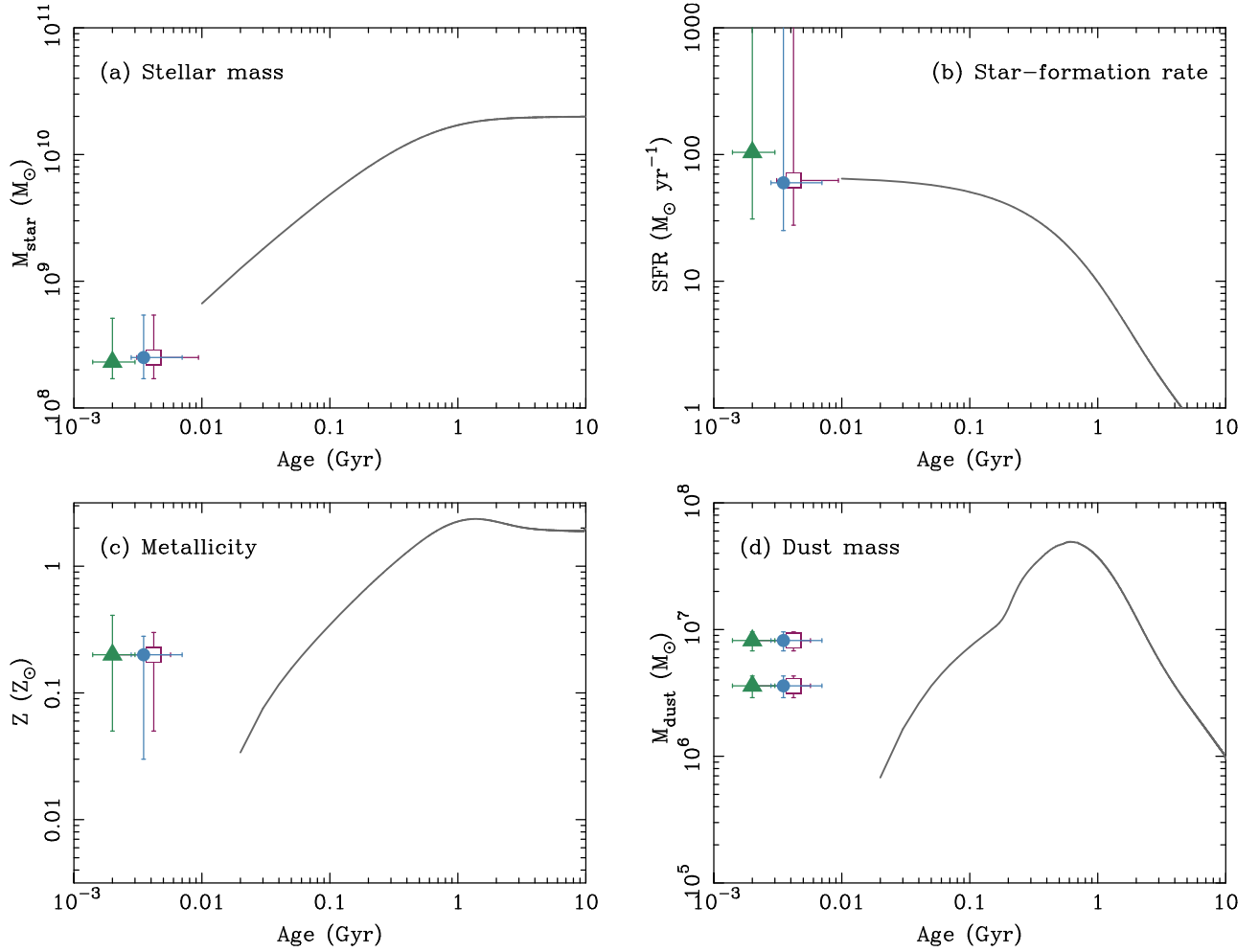
Figure 6. Time evolution of (a) stellar mass, (b) SFR, (c) metallicity, and (d) dust mass predicted in a dust formation model (Asano et al. 2013a, 2013b, 2014; Nozawa et al. 2015) as a function of galaxy age with an initial gas mass of $M_{gas} = 2 \times 10^{10} M_\odot$ and a star formation timescale of $\tau_{SFH} = 0.3$ Gyr. The open square, filled circle, and triangle represent the best-fitting parameters of the physical properties of MACS0416_Y1 estimated by the Calzetti, MW, and SMC extinction laws, respectively (see Table 5). In panel (d) two de-lensed dust mass estimates for $T_{dust} = 50$ K (lower symbols) and 40 K (upper symbols) are plotted.

In the $z > 7$ universe, SNe II ejecta with a typical dust yield per SN of $\gtrsim 0.1 M_\odot$ are claimed to be more important because at least some intermediate-mass and low-mass stars did not reach the AGB phase. In fact, large dust masses have been reported in some nearby young SN remnants (SNRs), which could explain the high dust yield (e.g., Dunne et al. 2003, 2009; Barlow et al. 2010; Matsuura et al. 2011, 2015; Gomez et al. 2012; Temim & Dwek 2013; Indebetouw et al. 2014; De Looze et al. 2017), although the other SNRs typically have much smaller dust masses of 10^{-3}–$10^{-2} M_\odot$ (Michałowski 2015, and references therein). It is likely that the discrepancy is due to the difference in the evolutionary phases of SNRs, in which most dust grains are destroyed by reverse shocks associated with the SN and do not survive in the later SNR phase (Micelotta et al. 2018, and references therein). If this is the case, it dramatically reduces the yield of dust grains per SN compared to previous beliefs. A top-heavy IMF is also claimed to explain a high dust yield per unit SFR (Gall et al. 2011), although this could lead to a higher rate of dust destruction by more frequent SN shocks. In recent years, a microscopic process of grain growth in dense ISM has been studied to overcome the problem of explaining the high-z dust reservoirs (e.g., Liffman & Clayton 1989; Dwek 1998; Draine 2009; Jones & Nuth 2011). In these models, accretion of gas-phase metal onto dust grains becomes more efficient in

dense molecular clouds (MCs) as the ISM is metal-polluted by stellar ejecta and eventually increases the dust mass for fixed SFR (e.g., Asano et al. 2013a; Zhukovska 2014), allowing one to require neither extreme dust yield per SN nor unusual IMFs.

Here, we employ a dust formation model developed by Asano et al. (2013a, 2013b, 2014) and Nozawa et al. (2015) to assess if the dust mass observed in MACS0416_Y1 is reproduced in the stellar age of ≈ 4 Myr. In this model, the time evolutions of masses of stars, ISM, metal, and dust are solved with four independent equations in which SFR, dust injection into (ejection from) stars, dust destruction by SNe, and grain growth in dense ISM are considered. The formation and destruction of dust grains are assumed to be processed in three phases of ISM; warm neutral media (WNM, $T_{gas} = 6000$ K, $n_H = 0.3$ cm^{-3}), cold neutral media (CNM, $T_{gas} = 100$ K, $n_H = 30$ cm^{-3}), and MCs ($T_{gas} = 25$ K, $n_H = 300$ cm^{-3}). We assume the mass fractions of WNM, CNM, and MC to be $(\eta_{WNM}, \eta_{CNM}, \eta_{MC}) = (0.5, 0.3, 0.2)$ following Nozawa et al. (2015). We use the IMF from Chabrier (2003). The star formation timescale is set to $\tau_{SFH} = 0.3$ Gyr, which is well within the 68% confidence intervals of the best-fitting τ_{SFH} (Table 5). The total baryon mass is scaled to $M_{tot} = 2 \times 10^{10} M_\odot$ such that the model stellar mass and SFR at the galaxy age of 4 Myr roughly match the best-fitting values

$M_{\rm star} = 3 \times 10^8\, M_\odot$ and SFR $= 60\, M_\odot\, {\rm yr}^{-1}$, respectively (Table 5). Note that except this scaling, we made no parameter optimization nor fine-tuning with respect to the best-fitting values obtained by the SED fits.

The results are shown in Figure 6. Although the model does not compute the physical properties at the earliest ages (<0.01 Gyr), the predicted stellar mass and SFR extrapolated from the dust evolution model with a single episode of star formation (Figures 6(a), (b)) are well aligned with the results from the SED analysis. The predicted metallicity is, however, much lower (Figure 6(d)), suggesting that the ISM fed to ongoing star formation is already metal-polluted by past star formation.

Furthermore, the model fails to reproduce the dust mass (Figure 6(d)) if assuming that the observed $M_{\rm dust}$ would be produced by the ongoing star formation traced by the rest-frame UV continuum and the [O III] 88 μm line. At the age of <0.1 Gyr, the predicted metallicity and dust mass increase almost linearly as the cumulative number of SNe II increases. At > 0.1 Gyr, the ISM is sufficiently metal-polluted and triggers a rapid interstellar growth of dust grains, resulting in nonlinear evolution of $M_{\rm dust}$ at $\tau_{\rm age} \sim \tau_{\rm SFH} = 0.3$ Gyr. The dust mass evolution peaks at $\tau_{\rm age} \sim 0.\,6$ Gyr and gives $M_{\rm dust}/M_{\rm star} \approx 3 \times 10^{-3}$ (similar to low-z normal star-forming galaxies, see also Section 5.2), which is followed by a $M_{\rm dust}$ decrement due to grain consumption for star formation at $\gtrsim 1$ Gyr. The galaxy age of ≈ 4 Myr is too short to reproduce the observed $M_{\rm dust}$, and any reasonable modification of the model cannot explain the dust mass.

6.2. Potential Coexistence of an Evolved Stellar Component

The disagreement discussed above should be mitigated if assuming the presence of an underlying "old" stellar component assembled during past star formation activity. In what follows, we show that there is at least one solution that reasonably explains the physical properties required to reproduce the observed dust mass without any substantial change in the SED shape.

As for a single episode of star formation starting with zero metallicity, the time evolution of metallicity only depends on the elapsed time since the episode started. From Figure 6(c), past star formation lasting for ≈ 0.1 Gyr is necessary to reach $Z \approx 0.2\, Z_\odot$. The dust evolution model also predicts that an initial gas mass of $1 \times 10^{10}\, M_\odot$ will produce a dust mass of $M_{\rm dust} \approx 5 \times 10^6\, M_\odot$ in 0.1 Gyr. This stellar population has a virtually constant SFR of $\approx 30\, M_\odot\, {\rm yr}^{-1}$ for the duration of 0.1 Gyr and attains a stellar mass of $M_{\rm star} = 3 \times 10^9\, M_\odot$.

This massive, old stellar component does not conflict with the best-fitting SED (Section 5.2), if the old component has stopped the star formation activity at a certain point of time in the past and then has been passively evolving for a time duration comparable to the lifetimes of OB stars ($\gtrsim 0.1$ Gyr). Figure 7 shows the predicted SED of the old component with $M_{\rm star} = 3 \times 10^9\, M_\odot$ built by constant star formation starting 0.3 Gyr ago and lasting for 0.1 Gyr, which exhibits the Balmer break due to the lack of OB stars. The UV continuum of the old component is much fainter than that of the best-fit stellar component presented in Section 5.2, suggesting that the addition of the old component does not substantially change the stellar SED in the rest-frame UV-to-optical. A similar star formation history is advocated to account for an excess in the rest-frame optical observed in MACS1149-JD (Hashimoto et al. 2018c) or the presence of dust in B14-65666 (Hashimoto et al. 2018a).
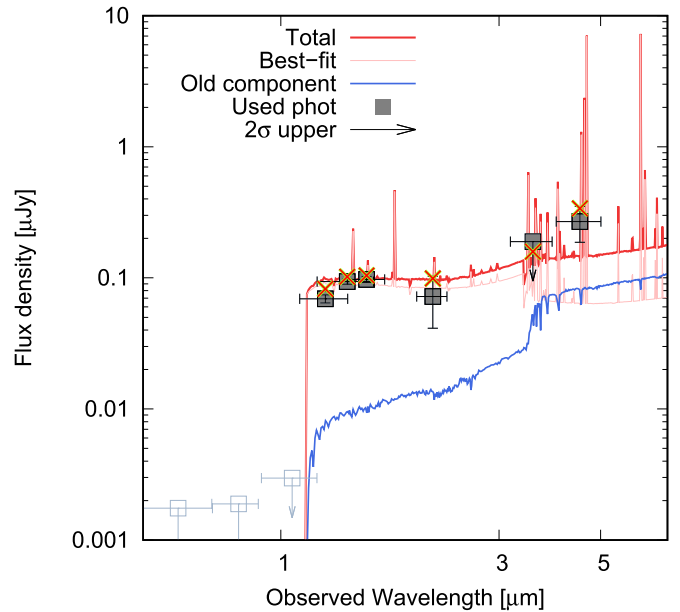
Figure 7. Stellar SED model (red curve) in which a mature ($\tau_{\rm age} = 300$ Myr) component with $M_{\rm star} = 3 \times 10^9\, M_\odot$ built by constant star formation lasting for 100 Myr (blue curve) is added to the best-fit SED model (pink curve, Section 5.2). The symbols are the same as those presented in Figure 5, but the crosses are flux densities predicted from the model in which the mature component is added. The open squares represent the photometric data at $<1\,\mu$m that are not used for SED fits. The extinction law is assumed to be Calzetti et al. (2000).

Therefore, it is likely that the mature (with an age of ~ 0.3 Gyr) stellar population with no or little ongoing star formation may be the origin of the very early enrichment of metal and dust.

7. Conclusions

We report ALMA detections of the [O III] 88 μm line and the 850 μm dust continuum emission in the Y-dropout LBG MACS0416_Y1 located behind the Frontier Field cluster MACS J0416.1−2403. Four independent tunings of ALMA were assigned to cover the contiguous frequency range between 340.0 and 366.4 GHz (a bandwidth of 26.4 GHz, corresponding to the redshift interval of $\Delta z = 0.72$ around $z \sim 8.5$), which reveals a spectroscopic redshift of $z = 8.3118 \pm 0.0003$. The observed 850 μm flux of $137 \pm 26\,\mu$Jy corresponds to the intrinsic IR luminosity of $L_{\rm IR} = 1.7 \times 10^{11}\, L_\odot$ if assuming a dust temperature of $T_{\rm dust} = 50$ K and emissivity index of $\beta = 1.5$, suggesting the fast assembly of a dust mass of $M_{\rm dust} = 4 \times 10^6\, M_\odot$ when the age of the universe was 600 Myr. The [O III] flux and the de-lensed luminosity are $F_{\rm [O\,III]} = 0.66 \pm 0.16$ Jy km s^{-1} and $L_{\rm [O\,III]} = (1.2 \pm 0.3) \times 10^9\, L_\odot$, respectively. The inferred [O III]-to-IR luminosity ratio of $\approx 1 \times 10^{-3}$ is comparable to those found in local dwarf galaxies, even if the uncertainty in dust temperature is taken into account. The rest-frame UV-to-FIR SED modeling where the [O III] emissivity model is incorporated suggests the presence of a young, but moderately metal-polluted stellar component with $M_{\rm star} = 3 \times 10^8 M_\odot$, $Z = 0.2 Z_\odot$, $\tau_{\rm age} = 4$ Myr. The analytic dust mass evolution model with $\tau_{\rm SFH} = 0.3$ Gyr, where interstellar grain growth and destruction are fully accounted for, does not reproduce the metallicity and the dust mass in a galaxy age of $\tau_{\rm age} = 4$ Myr, suggesting the presence of a past star formation episode as the origin of dust. We show that if a stellar population with past star formation triggered 0.3 Gyr ago and lasting for 0.1 Gyr is taken into account, it reproduces the

metallicity and the dust mass without any substantial change in the observed stellar SED.

The ionized and neutral ISM in MACS0416_Y1 are yet to be characterized completely. Rest-frame FIR and optical fine-structure lines such as [C II] 158 μm, [O I] 146 μm and [N II] 122/205 μm, and [O III] 52 μm and 4959/5007 Å, in addition to multi-wavelength photometry of the continuum emission, will offer a unique opportunity for a better understanding of the fundamental processes of metal/dust enrichment and star formation activity in MACS0416_Y1. Future ALMA and *JWST* observations of them will allow this to be investigated further.

Appendix
The Probability Distribution Functions (PDFs) of SED Fitting Parameters

Figures 8–10 show the PDFs for the SED fitting parameters. See Section 5.2 for details.
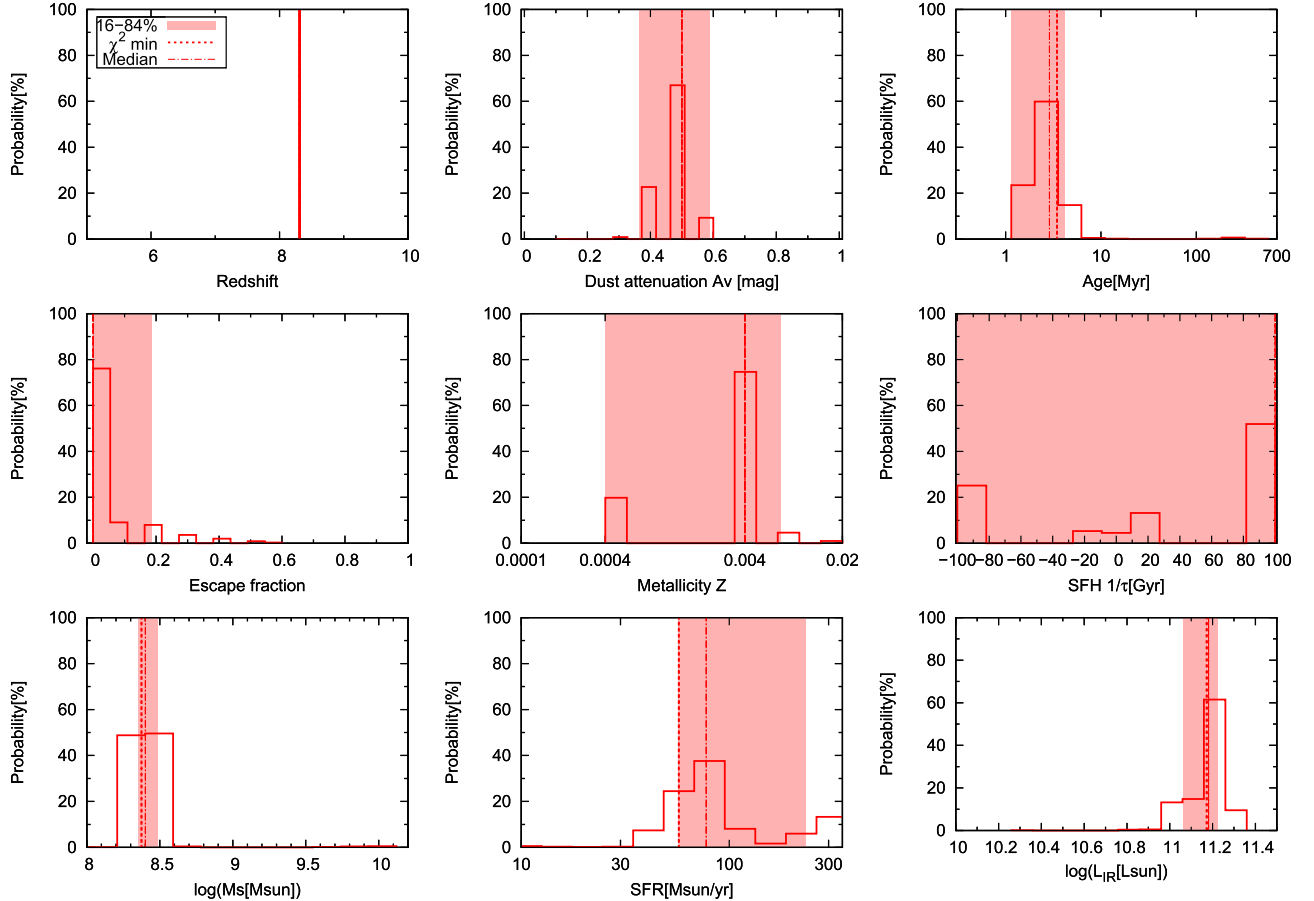
Figure 8. Probability distribution functions (PDFs) for the parameters employed in the SED fits presented in Section 5.2, such as the dust attenuation A_V, the galaxy age τ_{age}, the escape fraction of LyC photons f_{esc}, the metallicity Z, the star formation timescale τ_{SF}, the stellar mass M_{star}, SFR, and the infrared luminosity L_{IR}. The dotted and dashed–dotted lines represent the values that give the minimum-χ^2 and the median of the PDFs, respectively. The shaded areas show the 68% confidence intervals. The PDFs are obtained using the Calzetti extinction law.
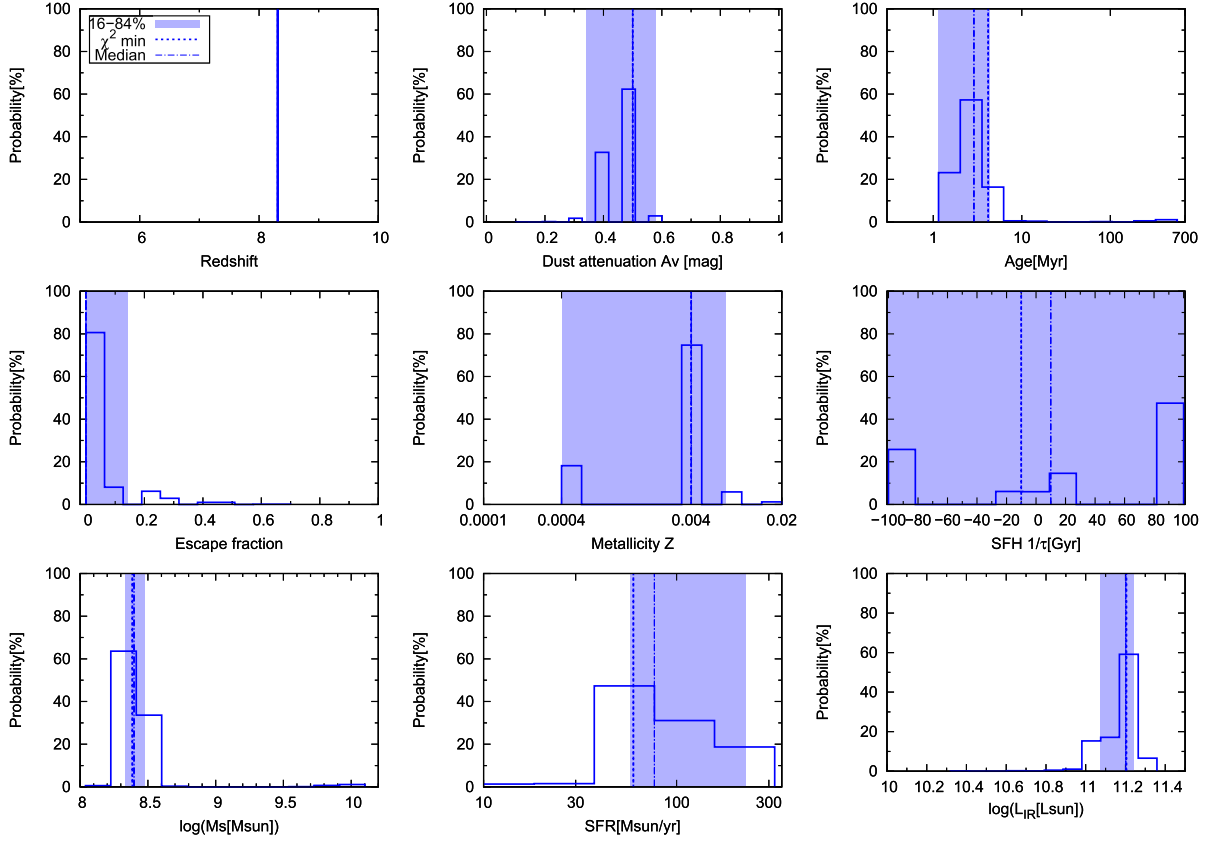
Figure 9. Same as Figure 8, but the probability distributions are obtained using the MW extinction law.
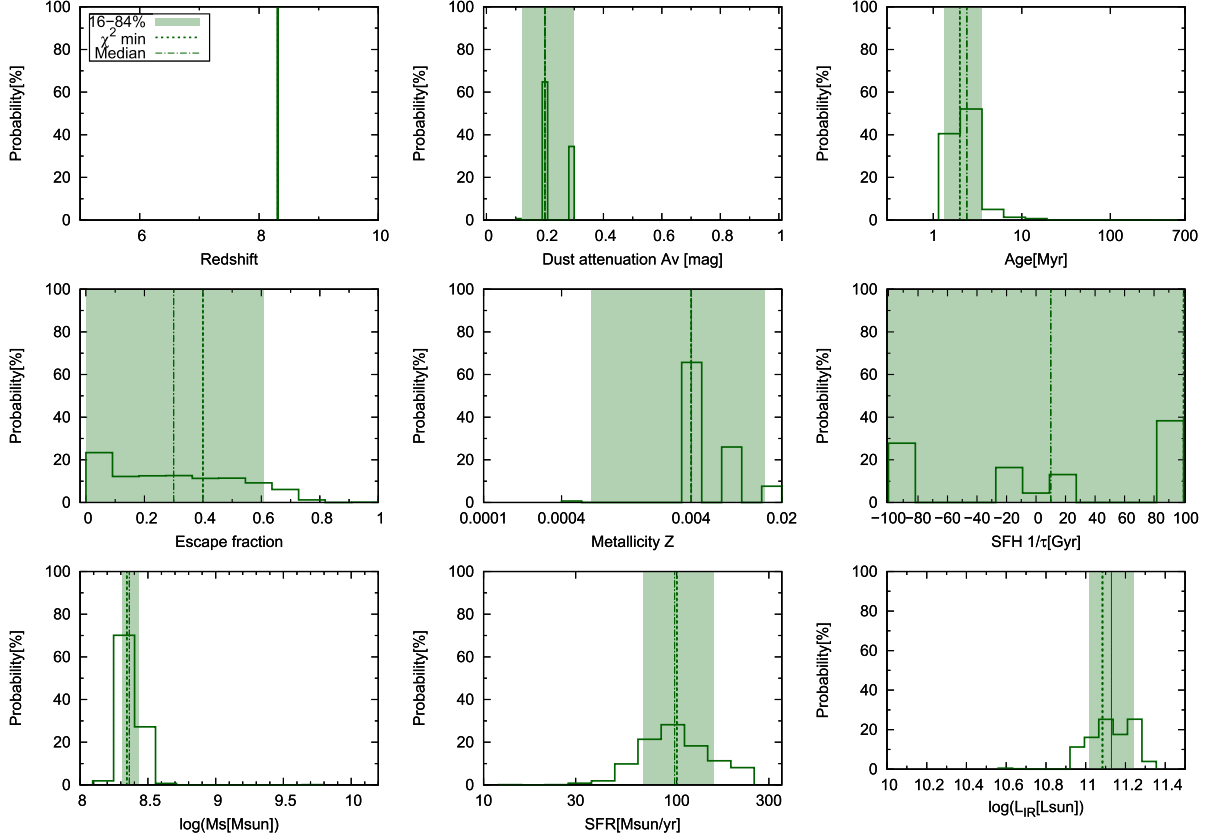
Figure 10. Same as Figure 8, but the probability distributions are obtained using the SMC extinction law.

ORCID iDs

Yoichi Tamura ⓘ https://orcid.org/0000-0003-4807-8117
Takuya Hashimoto ⓘ https://orcid.org/0000-0002-0898-4038
Akio K. Inoue ⓘ https://orcid.org/0000-0002-7779-8677
Erik Zackrisson ⓘ https://orcid.org/0000-0003-1096-2636
Lise Christensen ⓘ https://orcid.org/0000-0001-8415-7547
Naoki Yoshida ⓘ https://orcid.org/0000-0001-7925-238X
Minju M. Lee ⓘ https://orcid.org/0000-0002-2419-3068
Yoshiaki Taniguchi ⓘ https://orcid.org/0000-0003-2247-3741
Hideki Umehata ⓘ https://orcid.org/0000-0003-1937-0573
Bunyo Hatsukade ⓘ https://orcid.org/0000-0001-6469-8725
Kotaro Kohno ⓘ https://orcid.org/0000-0002-4052-2394
Kazuaki Ota ⓘ https://orcid.org/0000-0002-7675-5923

References

Asano, R. S., Takeuchi, T. T., Hirashita, H., & Inoue, A. K. 2013a, EP&S, 65, 213
Asano, R. S., Takeuchi, T. T., Hirashita, H., & Nozawa, T. 2013b, MNRAS, 432, 637
Asano, R. S., Takeuchi, T. T., Hirashita, H., & Nozawa, T. 2014, MNRAS, 440, 134
Barlow, M. J., Krause, O., Swinyard, B. M., et al. 2010, A&A, 518, L138
Bouchet, P., Lequeux, J., Maurice, E., Prevot, L., & Prevot-Burnichon, M. L. 1985, A&A, 149, 330
Bouwens, R. J., Illingworth, G. D., Oesch, P. A., et al. 2015, ApJ, 803, 34
Brammer, G. B., Marchesini, D., Labbé, I., et al. 2016, ApJS, 226, 6
Brauher, J. R., Dale, D. A., & Helou, G. 2008, ApJS, 178, 280
Bruzual, G., & Charlot, S. 2003, MNRAS, 344, 1000
Calzetti, D., Armus, L., Bohlin, R. C., et al. 2000, ApJ, 533, 682
Carniani, S., Maiolino, R., Pallottini, A., et al. 2017, A&A, 605, A42
Castellano, M., Amorín, R., Merlin, E., et al. 2016, A&A, 590, A31
Chabrier, G. 2003, PASP, 115, 763
Clark, C. J. R., Dunne, L., Gomez, H. L., et al. 2015, MNRAS, 452, 397
Cormier, D., Madden, S. C., Lebouteiller, V., et al. 2015, A&A, 578, A53
da Cunha, E., Eminian, C., Charlot, S., & Blaizot, J. 2010, MNRAS, 403, 1894
da Cunha, E., Groves, B., Walter, F., et al. 2013, ApJ, 766, 13
De Looze, I., Barlow, M. J., Swinyard, B. M., et al. 2017, MNRAS, 465, 3309
De Looze, I., Cormier, D., Lebouteiller, V., et al. 2014, A&A, 568, A62
De Vis, P., Dunne, L., Maddox, S., et al. 2017, MNRAS, 464, 4680
Díaz-Santos, T., Armus, L., Charmandaris, V., et al. 2017, ApJ, 846, 32
Draine, B. T. 2009, in ASP Conf. Ser. 414, Cosmic Dust—Near and Far, ed. T. Henning, E. Grün, & J. Steinacker (San Francisco, CA: ASP), 453
Draine, B. T., & Salpeter, E. E. 1979, ApJ, 231, 438
Dunne, L., Eales, S., Ivison, R., Morgan, H., & Edmunds, M. 2003, Natur, 424, 285
Dunne, L., Maddox, S. J., Ivison, R. J., et al. 2009, MNRAS, 394, 1307
Dwek, E. 1998, ApJ, 501, 643
Ferkinhoff, C., Hailey-Dunsheath, S., Nikola, T., et al. 2010, ApJL, 714, L147
Fitzpatrick, E. L., & Massa, D. 1986, ApJ, 307, 286
Gaia Collaboration, Brown, A. G. A., Vallenari, A., et al. 2016a, A&A, 595, A2
Gaia Collaboration, Prusti, T., de Bruijne, J. H. J., et al. 2016b, A&A, 595, A1
Gall, C., Hjorth, J., & Andersen, A. C. 2011, A&ARv, 19, 43
Gomez, H. L., Krause, O., Barlow, M. J., et al. 2012, ApJ, 760, 96
González-López, J., Bauer, F. E., Romero-Cañizales, C., et al. 2017, A&A, 597, A41
Hashimoto, T., Inoue, A. K., Mawatari, K., et al. 2018a, arXiv:1806.00486
Hashimoto, T., Inoue, A. K., Tamura, Y., et al. 2018b, arXiv:1811.00030
Hashimoto, T., Laporte, N., Inoue, A. K., et al. 2018c, Natur, 557, 392
Herrera-Camus, R., Sturm, E., Graciá-Carpio, J., et al. 2018a, ApJ, 861, 94
Herrera-Camus, R., Sturm, E., Graciá-Carpio, J., et al. 2018b, ApJ, 861, 95
Indebetouw, R., Matsuura, M., Dwek, E., et al. 2014, ApJL, 782, L2
Infante, L., Zheng, W., Laporte, N., et al. 2015, ApJ, 815, 18
Inoue, A. K. 2011a, MNRAS, 415, 2920
Inoue, A. K. 2011b, EP&S, 63, 1027
Inoue, A. K., Shimizu, I., Iwata, I., & Tanaka, M. 2014a, MNRAS, 442, 1805
Inoue, A. K., Shimizu, I., Tamura, Y., et al. 2014b, ApJL, 780, L18

Inoue, A. K., Tamura, Y., Matsuo, H., et al. 2016, Sci, 352, 1559
Ishigaki, M., Kawamata, R., Ouchi, M., et al. 2018, ApJ, 854, 73
Ivison, R. J., Swinbank, A. M., Swinyard, B., et al. 2010, A&A, 518, L35
Jones, A. P., & Nuth, J. A. 2011, A&A, 530, A44
Kausch, W., Noll, S., Smette, A., et al. 2015, A&A, 576, A78
Kawada, M., Takahashi, A., Yasuda, A., et al. 2011, PASJ, 63, 903
Kawamata, R., Oguri, M., Ishigaki, M., Shimasaku, K., & Ouchi, M. 2016, ApJ, 819, 114
Labbé, I., Oesch, P. A., Bouwens, R. J., et al. 2013, ApJL, 777, L19
Laporte, N., Ellis, R. S., Boone, F., et al. 2017, ApJL, 837, L21
Laporte, N., Infante, L., Troncoso Iribarren, P., et al. 2016, ApJ, 820, 98
Laporte, N., Streblyanska, A., Kim, S., et al. 2015, A&A, 575, A92
Liffman, K., & Clayton, D. D. 1989, ApJ, 340, 853
Lotz, J. M., Koekemoer, A., Coe, D., et al. 2017, ApJ, 837, 97
Madden, S. C., Rémy, A., Galliano, F., et al. 2012, in IAU Symp. 284, The Spectral Energy Distribution of Galaxies (Cambridge: Cambridge Univ. Press), 141
Madden, S. C., Rémy-Ruyer, A., Galametz, M., et al. 2013, PASP, 125, 600
Mainali, R., Zitrin, A., Stark, D. P., et al. 2018, MNRAS, 479, 1180
Maiolino, R., Carniani, S., Fontana, A., et al. 2015, MNRAS, 452, 54
Marrone, D. P., Spilker, J. S., Hayward, C. C., et al. 2018, Natur, 553, 51
Matsuura, M., Dwek, E., Barlow, M. J., et al. 2015, ApJ, 800, 50
Matsuura, M., Dwek, E., Meixner, M., et al. 2011, Sci, 333, 1258
Mawatari, K., Yamada, T., Fazio, G. G., Huang, J.-S., & Ashby, M. L. N. 2016, PASJ, 68, 46
McLeod, D. J., McLure, R. J., Dunlop, J. S., et al. 2015, MNRAS, 450, 3032
McMullin, J. P., Waters, B., Schiebel, D., Young, W., & Golap, K. 2007, in ASP Conf. Ser. 376, Astronomical Data Analysis Software and Systems XVI, ed. R. A. Shaw, F. Hill, & D. J. Bell (San Francisco, CA: ASP), 127
Micelotta, E. R., Matsuura, M., & Sarangi, A. 2018, SSRv, 214, 53
Michałowski, M. J. 2015, A&A, 577, A80
Modigliani, A., Goldoni, P., Royer, F., et al. 2010, Proc. SPIE, 7737, 773728
Nozawa, T., Asano, R. S., Hirashita, H., & Takeuchi, T. T. 2015, MNRAS, 447, L16
Oesch, P. A., Bouwens, R. J., Illingworth, G. D., Labbé, I., & Stefanon, M. 2018, ApJ, 855, 105
Oesch, P. A., Brammer, G., van Dokkum, P. G., et al. 2016, ApJ, 819, 129
Planck Collaboration, Aghanim, N., Akrami, Y., et al. 2018, arXiv:1807.06209
Postman, M., Coe, D., Benítez, N., et al. 2012, ApJS, 199, 25
Prevot, M. L., Lequeux, J., Maurice, E., Prevot, L., & Rocca-Volmerange, B. 1984, A&A, 132, 389
Rémy-Ruyer, A., Madden, S. C., Galliano, F., et al. 2015, A&A, 573, C1
Rieke, G. H., Alonso-Herrero, A., Weiner, B. J., et al. 2009, ApJ, 692, 556
Seaton, M. J. 1979, MNRAS, 187, 73P
Shimizu, I., Inoue, A. K., Okamoto, T., & Yoshida, N. 2014, MNRAS, 440, 731
Smit, R., Bouwens, R. J., Franx, M., et al. 2015, ApJ, 801, 122
Smith, D. J. B., Dunne, L., da Cunha, E., et al. 2012, MNRAS, 427, 703
Stark, D. P. 2016, ARA&A, 54, 761
Stark, D. P., Ellis, R. S., Charlot, S., et al. 2017, MNRAS, 464, 469
Stark, D. P., Richard, J., Charlot, S., et al. 2015a, MNRAS, 450, 1846
Stark, D. P., Walth, G., Charlot, S., et al. 2015b, MNRAS, 454, 1393
Takami, H., Maihara, T., Mizutani, K., et al. 1987, PASP, 99, 832
Temim, T., & Dwek, E. 2013, ApJ, 774, 8
Tody, D. 1993, in ASP Conf. Ser. 52, Astronomical Data Analysis Software and Systems II, ed. R. J. Hanisch, R. J. V. Brissenden, & J. Barnes (San Francisco, CA: ASP), 173
Valtchanov, I., Virdee, J., Ivison, R. J., et al. 2011, MNRAS, 415, 3473
Venemans, B. P., McMahon, R. G., Walter, F., et al. 2012, ApJL, 751, L25
Venemans, B. P., Walter, F., Decarli, R., et al. 2017, ApJL, 851, L8
Vernet, J., Dekker, H., D'Odorico, S., et al. 2011, A&A, 536, A105
Vishwas, A., Ferkinhoff, C., Nikola, T., et al. 2018, ApJ, 856, 174
Walter, F., Riechers, D., Novak, M., et al. 2018, ApJL, 869, L22
Watson, D., Christensen, L., Knudsen, K. K., et al. 2015, Natur, 519, 327
Weingartner, J. C., & Draine, B. T. 2001, ApJ, 548, 296
Zheng, W., Zitrin, A., Infante, L., et al. 2017, ApJ, 836, 210
Zhukovska, S. 2014, A&A, 562, A76
Zhukovska, S., Gail, H.-P., & Trieloff, M. 2008, A&A, 479, 453
Zitrin, A., Ellis, R. S., Belli, S., & Stark, D. P. 2015a, ApJL, 805, L7
Zitrin, A., Labbé, I., Belli, S., et al. 2015b, ApJL, 810, L12